Analysis of the interaction between turbulent combustion and thermal radiation using unsteady coupled LES/DOM simulations.

POITOU Damien (poitou@cerfacs.fr)[a], AMAYA Jorge[a], EL HAFI Mouna[b], CUENOT Bénédicte[a]

[a] *CERFACS, 42, Avenue Gaspard Coriolis, 31057 Toulouse Cedex 01, France.*
[b] *Centre RAPSODEE, École des Mines d'Albi, Campus Jarlard, 81013 Albi, France*

Abstract

Radiation exchanges must be taken into account to improve the prediction of heat fluxes in turbulent combustion. The strong interaction with turbulence and its role on the formation of polluting species requires the study of unsteady coupled calculations using Large Eddy Simulations (LES) of the turbulent combustion process. Radiation is solved using the Discrete Ordinate Method (DOM) and a global spectral model. A detailed study of the coupling between radiative heat transfer and LES simulation involving a real laboratory flame configuration is presented. First the impact of radiation on the flame structure is discussed: when radiation is taken into account temperature levels increase in the fresh gas and decrease in the burnt gas, with variations ranging from 100K to 150K thus impacting the density of the gas. Coupling DOM and LES allows to analyse radiation effects on flame stability: temperature fluctuations are increased and a wavelet frequency analysis shows changes in the flow characteristic frequencies. The second part of the study focuses on the Turbulence Radiation Interaction (TRI) using the instantaneous radiative fields on the whole computational domain. TRI correlations are calculated and are discussed along 4 levels of approximation. The LES study shows that all the TRI correlations are significant and must be taken into account. These correlations are also usefull to calculate the TRI correlations in the Reynolds Averaged Navier-Stokes (RANS) approach.

Keywords: Turbulent combustion, Large Eddy Simulation, Radiative transfer, Spectral models, Discrete ordinate method (DOM), Coupling,

Turbulence-Radiation Interaction (TRI).

1. Introduction

Besides combustion efficiency, the design of industrial combustion chambers and furnaces is strongly dictated by thermal constraints. The solid parts of a combustor are made of materials that do not support a direct contact with the high temperature burnt gases. As a consequence chamber walls must be cooled down, using complex cooling techniques that are expensive to design, develop and operate. The inclusion of such systems modifies the temperature distribution inside the chamber and hence the turbulent combustion. The thermal behavior of a combustion chamber is also critical for the downstream elements (turbines): thermal constraints of the materials, impose strict limits on the temperature levels and fluctuations in the incoming flow exiting from the combustion chamber. Finally, thermal behaviour also has an impact on the production of pollutants such as CO, NO_x and soot, and may modify the interaction of impinging fuel droplets with the walls.

The mean temperature level in a combustion chamber is well estimated, at first order, by a simple enthalpy balance between fresh reactants and hot products. If NO_x and soot are not produced, neglecting radiation and wall temperature variations still leads to relatively accurate mean temperature levels but is responsible of errors on temperature fluctuations. The inclusion of pollutants emission re-enforces this error and introduces a deviation of the mean temperature. Such error levels are outside the tolerance range for combustor design and it is therefore necessary to include radiation in combustion studies for the optimization of combustion chambers.

In this process, numerical simulation plays an increasingly important role. In comparison with experimental setups, numerical simulation shows the advantage of being cheaper and more flexible. Its main drawback is its use of models to represent limited accuracy of the numeric complex physics. Important progress however have been made in the last years, in particular with the development of the Large Eddy Simulation (LES) approach and the sustained increase of computational power. Today LES is routinely applied to industrial burners and gives accurate and reliable solutions, as demonstrated in the recent literature [1, 2, 3]. Computational power has also been used in recent time to calculate radiation in complex geometries [4, 5, 6].

Radiation is a complex, non-local phenomenon in which energy is simultaneously emitted and absorbed by the gases. To correctly capture the effect of radiation, both emission and absorption must be included and coupled with combustion. This is the aim of the present work, where unsteady combustion-radiation simulations of a laboratory burner have been performed. The main objectives of this work consist in the validation of the coupling methodology, the quantification and analysis of the interaction between the involved phenomena and the evaluation of the impact of radiation on the thermal behavior of the burner. To perform such coupled simulations high performance computing techniques must be used, as well as a reliable coupling methodology, which are an important challenge: a demonstration of the feasibility and the importance of such simulations is a main objective of this paper.

The present document is organized in four main parts: section 2 presents the basics aspects of the computational methods for unsteady turbulent combustion and radiative heat transfer, and shows a description of the unsteady coupling methodology. In section 3 the configuration and the simulation set up is presented. Results are analyzed in sections 4 to 6, first by comparing the uncoupled and the coupled simulations, then by a detailed description of the interaction between turbulence and radiation. Finally in section 7 a summary the main findings of this study is presented.

2. Modelling of coupled LES and Radiative Calculation

2.1. LES equations

The conservation equations of the fluid can be written in a matrix form:

$$\frac{\partial \mathbf{w}}{\partial t} + \nabla \cdot \underline{\mathbf{F}} = \mathbf{s} \tag{1}$$

where $\mathbf{w} = (\rho u, \rho v, \rho w, \rho E, \rho Y_k)^T$ is the conservative variable vector that is solved at each location $\mathbf{x}$ and time t, with ρ the mixture density, u, v, w the components of the velocity vector $\mathbf{v}$, E the energy density and Y_k the mass fraction of the specie k ($1 \leq k \leq N_{\text{species}}$). The flux tensor $\underline{\mathbf{F}}$ can be decomposed in a inviscid (noted I) and a viscous component (noted V):

$$\underline{\mathbf{F}}^I = \begin{bmatrix} \mathbf{v} : \rho \mathbf{v}^T + P \\ (\rho E + P)\mathbf{v} \\ \rho_k Y_k \mathbf{v} \end{bmatrix} \underline{\mathbb{1}} \qquad (2) \qquad \text{and} \qquad \underline{\mathbf{F}}^V = \begin{bmatrix} -\underline{\tau} \\ -\mathbf{v}^T \cdot \underline{\tau} + \mathbf{q} \\ \mathbf{J}_k \end{bmatrix} \qquad (3)$$

using the hydrodynamic pressure P defined by the equation of state of perfect gas, $\mathbf{q}$ the heat flux and $\mathbf{J_k}$ the diffusive flux of species k. The stress tensor for a Newtonian fluid $\underline{\tau} = [\tau_{ij}]$ is:

$$\tau_{ij} = 2\mu \left(S_{ij} - \frac{1}{3}\delta_{ij} S_{ll} \right) \qquad \text{where} \qquad S_{ij} = \frac{1}{2}\left(\frac{\partial u_j}{\partial x_i} + \frac{\partial u_i}{\partial x_j} \right) \tag{4}$$

For a reacting flow including radiation, the source term $\mathbf{s}$ is written:

$$\mathbf{s} = (0, 0, 0, \dot{\omega}_T + S_r, \dot{\omega}_k)^T \tag{5}$$

where $\dot{\omega}_T$ is the chemical heat release, S_r is the thermal radiative heat source and $\dot{\omega}_k$ is the reaction rate for species k.

A Favre filtering (defined in Eq. 6) is used to derive the filtered balance equations for LES (Eq. 7) are obtained from equations (Eq. 1), assuming a commutation between the filter and derivative operator[7]:

$$\widetilde{\phi} = \frac{\overline{\rho\phi}}{\overline{\rho}} \tag{6}$$

$$\frac{\partial \bar{\mathbf{w}}}{\partial t} + \nabla \cdot \underline{\bar{\mathbf{F}}} = \bar{\mathbf{s}} \tag{7}$$

The filtered flux tensor $\underline{\bar{\mathbf{F}}}$ contains a resolved part, expressed by Eq. (2) and Eq. (3) using filtered variables, and an unresolved part which is modeled in the form of a subgrid flux tensor $\underline{\mathbf{F}}^t$:

$$\underline{\mathbf{F}}^t = \begin{bmatrix} -\underline{\tau}^t \\ \mathbf{q}^t \\ \mathbf{J}_k^t \end{bmatrix} \tag{8}$$

where

$$\tau_{ij}^t = -\ \overline{\rho}(\widetilde{u_i u_j} - \widetilde{u}_i \widetilde{u}_j) \tag{9}$$

$$q_i^t = \overline{\rho}(\widetilde{u_i E} - \widetilde{u}_i \widetilde{E}) \tag{10}$$

$$J_{i,k}^t = \overline{\rho}(\widetilde{u_i Y_k} - \widetilde{u}_i \widetilde{Y}_k) \tag{11}$$

Note that the subgrid Reynolds stress tensor $\underline{\tau}^t$, the subgrid turbulent heat flux $\mathbf{q}^t$ and the subgrid turbulent species flux $\mathbf{J}_k^t$ model the unresolved convective transport only. Unresolved diffusive transport is neglected.

Momentum, energy and species conservation equations are solved using realistic thermochemistry, *i.e.* real values for all thermodynamic properties taken from reference databases for each chemical species. The subgrid model describing the turbulent stress tensor (Eq. 9) is based on the turbulent viscosity concept using the WALE model [8, 9]. Turbulent fluxes for thermal and species diffusion (Eqs. 11 and 10) are modeled by classical gradient laws with turbulent Schmidt and Prandtl numbers. Characteristic boundary con-

ditions NSCBC [10] are used for all inlets and for the outlet allowing the evacuation of acoustic energy from the domain.

The numerical calculation was performed with the unstructured compressible Navier-Stokes solver AVBP[1], using a 3rd order in space and time Taylor-Galerkin scheme (TTGC [11]).

2.2. Turbulent Combustion Modeling

The turbulent flame front is described using the dynamic Thickened Flame Model (TFLES). In such a model the reaction front is artificially thickened in order to solve stiff gradients on the grid without altering global flame characteristics. This model is detailed in [12] and has been extensively used and validated in numerous configurations [1, 3, 2]. Subgrid wrinkling is modeled using an efficiency function [12]. In the present configuration, the maximum thickening factor is $F_{max} = 20$. A priori tests based on Direct Numerical Simulations [12] and a posteriori evaluation of the TFLES model on complex configurations have shown that the thickening factor should not be too large to stay in the limit of the model assumptions and that a value of 20 is reasonable.

The chemistry (*i.e.* Eq. 12 and 13) of propane/air combustion is computed using a two-step mechanism [13] designed to give the correct flame speed and temperature. The TFLES model evaluates the reaction rates $\overline{\dot{\omega}_i}$ for both reactions with Arrhenius laws (Eqs. (14) and (15)) using LES filtered values (denoted with a tilde) of the mass fractions and temperature.

$$C_3H_8 + \frac{7}{2}O_2 \quad \Rightarrow \quad 3CO + 4H_20 \tag{12}$$

$$CO + \frac{1}{2}O_2 \quad \Leftrightarrow \quad CO_2 \tag{13}$$

$$\overline{\dot{\omega}_1} \quad = A_1[\widetilde{C_3H_8}]^{\alpha_1}[\widetilde{O_2}]^{\beta_1}\exp(-E_{a_1}/R\widetilde{T}) \tag{14}$$

$$\overline{\dot{\omega}_2} \quad = A_2[\widetilde{CO_2}]^{\alpha_2}[\widetilde{O_2}]^{\beta_2}\exp(-E_{a_2}/R\widetilde{T}) \tag{15}$$

2.3. Thermal Radiation Modeling

Radiative heat transfer is solved via the Radiative Transfer Equation (RTE) discretized with the Discrete Ordinates Method (DOM) for unstruc-

[1] `http://www.cerfacs.fr/4-26334-The-AVBP-code.php`

tured hybrid meshes [14, 4, 15, 16, 5]. The RTE is solved in its differential form (Eq. (16)), for a non scattering medium, with the associated boundary conditions (Eq (17)):

$$\mathbf{s} \cdot \nabla L_\nu(\mathbf{x}, \mathbf{u}) = \kappa_\nu \left[L^0_\nu(\mathbf{x}) - L_\nu(\mathbf{x}, \mathbf{u}) \right] \quad (16)$$

$$L_\nu(\mathbf{x}_w, \mathbf{u}) = \underbrace{\epsilon_\nu(\mathbf{x}_w) L^0_\nu(\mathbf{x}_w)}_{\text{Emitted part}} + \underbrace{\rho_\nu(\mathbf{x}_w) L_{\nu,incident}(\mathbf{x}_w, \mathbf{u})}_{\text{Reflected part}} \quad (17)$$

where ν is the wavenumber, $L_\nu(\mathbf{x}, \mathbf{u})$ is the incident intensity at the point $\mathbf{x}$ in the direction $\mathbf{u}$ and κ_ν is the absorption coefficient, $\epsilon_\nu(\mathbf{x}_w)$ is the wall emissivity and $\rho_\nu(\mathbf{x}_w)$ the wall reflectivity with $\rho_\nu(\mathbf{x}_w) = 1 - \epsilon_\nu(\mathbf{x}_w)$. L^0_ν is the equilibrium Planck function.

To accurately calculate the wall temperature, which is critical for radiation, a conductive heat transfer process should be included [6]. To simplify the problem, all the walls are here assumed to be isothermal at an arbitrary constant cold temperature ($T_w = 300\ K$), as no measurements are available. This may lead to over estimate the radiative heat losses but still allows to validate the coupling methodology and to analyse the coupled interactions between thermal radiation and turbulent combustion.

The source term S_r injected in the energy balance equation of the flow results from a double integration of the RTE over the solid angle and the gas spectra, and depends only on the position $\mathbf{x}$:

$$S_r(\mathbf{x}) = \int_0^\infty \kappa_\nu \left[4\pi L^0_\nu(\mathbf{x}) - \int_{4\pi} L_\nu(\mathbf{x}, \mathbf{u}) d\Omega \right] d\nu \quad (18)$$

This double integration is performed in the solver PRISSMA[2] based on the following discretization:

- Angular discretization: the Discrete Ordinate Method (DOM), a finite volume method (FVM) formulation of the RTE, offers a good compromise between accuracy and CPU time [14, 16, 17]. The RTE is solved for a set of N_{dir} directions (ordinates) by using a S_n quadrature (with $N_{dir} = n(n+2)$) [18] or a LC_{11} quadrature (where $N_{dir} = 96$) [19]. The Diamond Mean Flux Scheme (DMFS) is used for the spatial integration

[2]PRISSMA: Parallel RadIation Solver with Spectral integration on Multicomponent mediA, `http://www.cerfacs.fr/prissma`

[15].

- Spectral integration: the spectral properties of absorbing gases such as CO, CO_2 and H_2O are known but very complex. Spectroscopic data cover wavelengths in the range $\nu = [150; 9300]\ cm^{-1}$ and give gas properties for 367 narrow bands of width $\Delta\nu_i = 25\ cm^{-1}$ [20]. Four additional bands $\nu = [9300; 20000]\ cm^{-1}$ are added to the visible spectrum to evaluate the radiation of soot.

  Narrow-band models such as SNB-CK [21, 22] offer a good accuracy with a 5 points Gauss-Legendre quadrature. Over 371 bands this leads to 1855 resolutions of the RTE per direction. This is far too costly to handle complex geometries in unsteady calculations and global models are preferred, which reduce the calculation to only 3 to 15 spectral integrations in each direction. In PRISSMA different spectral models are available: SNB-CK, SNB-FSK [23], SNB-FSCK [24] and WSGG [25].

  The SNB-FSCK model is one order of magnitude faster than SNB-CK model for results of the same accuracy. As most of the computational time is used in the calculation of the absorption coefficients, they are pre-calculated in a table which allows to achieve a performance close to a classical WSGG model with a much higher accuracy. If the pressure is assumed constant, absorption coefficients can be tabulated in a four-dimensional space including temperature and H_2O, CO_2 and CO [5]. The retained spectral model consists on a tabulated SNB-FSCK approach.

The spatial discretization may impact the so-called Turbulence Radiation Interaction (TRI) [26] and requires a subgrid scale model for radiation. Using filtered Direct Numerical Simulation (DNS), Poitou *et al.* [27, 5] showed that the subgrid scale temperature and composition fluctuations have a small effect on the emitted radiation. This result has been confirmed by Coelho and Roger *et al.*, who studied both emission and absorption TRI at the subgrid scale [28, 29, 30]. As the flame is artificially thickened by the TFLES model the optical thickness of the flame front may be modified: it has been shown [5] however that this effect can be neglected. Therefore it can be assumed that:

$$\overline{S_r(T, X_i, p)} \simeq S_r(\widetilde{T}, \widetilde{X_i}, \widetilde{p}) \tag{19}$$

2.4. Coupling Methodology

In a coupled combustion/radiation calculation, the radiative source term S_r must be known in the fluid solver while the radiative solver needs the local temperature, pressure and molar fractions of radiating species (H_2O, CO_2, CO and possibly soot) in the fluid. Because of the double integration over directions and frequencies, the CPU cost of the radiative solver is much more important than the CFD slover. The coupling methodology has been presented and validated in a preceding paper [31], where both solvers run simultaneously and use the data obtained at the previous coupling iteration[32, 33]. This requires synchronization both in physical and CPU time:

- Synchronization in physical time: radiation and combustion have different characteristic time steps. The LES time step Δt_{LES} is fixed by the CFL criterion for the propagation of acoustic waves (compressible flows) :

$$\Delta t_{LES} = \frac{\mathrm{CFL} \times \Delta x_{min}}{c_s} \tag{20}$$

  where Δx_{min} is the smallest mesh size and c_s is the local speed of sound. For an explicit code like AVBP, a $CFL = 0.7$ is required, typically leading to $\Delta t_{LES} \approx 1\ \mu s$. Radiation is an instantaneous phenomenon and therefore evolves with the convection time scale of gas [34, 35]:

$$\tau_f = \frac{\Delta x_{min}}{\overline{u}} \tag{21}$$

  where $\overline{u}$ is the bulk flow velocity.

  It is convenient to introduce a coupling frequency N_{it} which represents the number of LES iterations between two radiation calculations. Ideally $N_{it} \times \Delta t_{LES} = \tau_f$, leading to:

$$N_{it} = \frac{\tau_f}{\Delta t_{LES}} = \frac{c_s}{\mathrm{CFL} \times \overline{u}} = \frac{1}{\mathrm{CFL} \times M} \tag{22}$$

  where M is the Mach number. For the low-Mach flows considered here, $N_{it} \sim 100$ is typically obtained. The effect of the coupling frequency has also been studied by Dos Santos *et al.* [36, 37] who also retained $N_{it} = 100$.

- Sychronization in CPU time: the computational time necessary to perform one radiation calculation must be equal to the time necessary to perform N_{it} LES iterations:

$$N_{it} \times t_{LES}^{CPU} = t_{Rad}^{CPU} \tag{23}$$

where t_{LES}^{CPU} and t_{Rad}^{CPU} are respectively the CPU time required for one fluid iteration and one radiative calculation.

Radiation models and discretizations have been evaluated in [31] in terms of accuracy vs CPU time. This allowed to identify optimal choices for the angular quadrature, the spectral model and the spatial/temporal discretization. In addition mesh coarsening based on temperature distribution [31] reduced calculation time and memory allocation for radiation. Finally a tabulated global model SNB-FSCK with an S_4 quadrature was used on the coarsen mesh. This allowed to reach a CPU time ratio PRISSMA/AVBP close to one (*i.e.* with $P_{LES} = P_{Rad}\ N_{it} \times t_{LES}^{CPU}/t_{Rad}^{CPU} \approx 0.6$) and ensured CPU time synchronisation with an acceptable accuracy.

The data exchange, communications and resource distribution between PRISSMA and AVBP is handled by a coupler O-PALM[3], initially developed at CERFACS for meteorological applications [38]. It is used to run the two codes AVBP and PRISSMA on P_{LES} and P_{Rad} processors respectively. A third code called "bridge" is used to handle the interpolation of physical data from AVBP to PRISSMA. The total number of processors is $P = P_{LES} + P_{Rad} + 2$, where two additional processors are used for the coupler driver and for the bridge (Fig. 2).

The restitution time (*i.e.* wall clock time calculation for one solution) depends on the code efficiency and the allocated number of processors. AVBP is parallelized with a domain decomposition which is very efficient on massively parallel architectures with a perfect speed-up factor up to 4 078 processors on IBM BlueGene/L [39]. In the radiation calculation, the integral of the incident intensity involves the whole domain so that the use of domain decomposition is not straightforward. PRISSMA uses two levels of parallelism: directional and spectral. For an S_4 quadrature with 15 spectral quadrature points the maximum number of processor is 360, but the parallel efficiency

[3]O-PALM: `http://www.cerfacs.fr/globc/PALM_WEB`

is limited (around 30% for the maximum number of processors). This is an important limitation for coupled simulations on industrial configurations and the use of domain decomposition for radiation is currently an issue which is under investigation.

Following the above strategy, the 132 processors of a SGI Altix ICE computer have been optimally distributed using: 106 processor for AVBP, 24 for PRISSMA and 2 processors for O-PALM and the Bridge. This set-up gives a restitution time of 38.6 s for 100 iterations of AVBP and 37.2 s for PRISSMA, *i.e.* a well balanced coupling.

3. Configuration

3.1. Geometry

The study case corresponds to an experiment developed and initially analysed by Knikker *et al.* [40, 41, 42] (Fig. 1). A premixed propane/air flow is injected into a rectangular chamber, of dimensions 50, 80 and 400 mm in height, depth and length respectively. Lateral walls are transparent artificial quartz windows to allow visualisation of the flame. The upper and the lower walls are made of ceramic material for thermal insulation and also include quartz windows to introduce LASER sheets for measurements (cf. Fig. 1).

A stainless steel triangular flame holder is fixed to lateral windows, measuring 25 mm in height which corresponds to a 50% blockage ratio. The V-shaped turbulent flame is stabilized by the flow velocity recirculating zone behind the flame holder.

Inlet conditions are given for the propane/air mixture with a velocity of 5 m.s^{-1}, a temperature of 300 K with an equivalent ratio of $\phi = 1$ and a turbulence level about 5%. Outlet condition is at atmospheric pressure.

3.2. Simulation set up

In the simulation, the inlet is placed 10 cm upstream the flame holder and the chamber is 30 cm long. A 3D box of $30 \times 30 \times 30$ cm is added at the outlet of the chamber to emulate the atmosphere. The mesh contains about 4.7 millions tetrahedra. The cell size is about 1 mm, for the smallest cells close to the obstacle, and then increases progressively towards the exit of the chamber. To guarantee a non-disturbing outlet boundary condition, a nitrogen coflow at 20 m.s^{-1} and 1900 K is added at the left-most limit of the atmosphere thus avoiding recirculation in the atmosphere and at the outlet.

The walls of the chamber are not isothermal : their wall temperature is the result of heat transfer through the solid between the interior and the exterior of the chamber. In the present simulation this is modelled using a wall thermal resistance of $R_{th} = 0.096$ K.m^2.W^{-1} for the ceramic walls (upper and lower), $R_{th} = 0.086$ K.m^2.W^{-1} for quartz windows (front and behind) and $R_{th} = 120$ K.m^2.W^{-1} for the flame holder [37]. The heat loss at the wall is calculated as:

$$q_{wall} = \frac{1}{R_{th}}(T_{ref} - T_{wall}) \tag{24}$$

with $T_{ref} = 300K$ and T_{wall} the fluid temperature near the wall. The walls around the atmosphere at the end of the chamber are adiabatic slip walls.

In the radiative solver the walls are however assumed isothermal with $T_w = 300\ K$ except for the coflow which is at $T_w = 1900\ K$. As discussed previously this is not consistent with the thermal wall loss in the fluid solver, and the conduction in the solid should be calculated.

4. Results

4.1. Flow

LES results have been compared against experimental data in [37, 5] and showed a good agreement. Mean fields were obtained after time averaging over 46.23 ms for the uncoupled solution and over 39 ms for the coupled calculation.

Fig. 3 shows the temperature and the velocity fields in the plane $z = 0$ for the uncoupled LES calculation. The velocity fields show a recirculation zone behind the flame holder where the trapped hot gas stabilize the flame. RMS fields show high levels close to the wall caused by the flame quenching and reigniting to consume the remaining unburnt fuel.

The time averaged fields of mass fractions of radiating species (H_2O, CO_2 and CO) in the plane $z = 0$ are plotted in Fig. 4. A large amount of CO is produced at the end of the chamber. The mass fraction of CO is more important than in adiabatic conditions due to the thermal wall law loss. As the second chemical reaction in Eq. 13 is reversible, the thermal losses shift the equilibrium backwards. The large amount of CO is localized where the second equilibrium (Eq. (15)) is reversed. The contour observed on Y_{CO} in Fig. 4 represents the line where the net second reaction rate is zero. In the chemical mechanism used here, the second reaction is endothermic and allows

to obtain the right flame speed and temperature under adiabatic conditions. It use in non-adiabatic conditions with heat loss must be taken with care: the increase of CO with thermal loss is probably not realistic.

4.2. Influence of radiation on turbulent combustion: comparison of coupled and uncoupled calculation

The total energy released by the combustion in the chamber in the coupled calculation is 75.04 kW. The total net radiative energy is about 1.8 kW, *i.e.* only 2.3% of the combustion energy. The radiative effect on the mean flow is therefore a second order effect. However previous studies [36, 37] have shown that this effect may still be important, in particular by increasing the flow fluctuations. Note that the radiated energy is not equal to the heat release difference between the coupled and uncoupled calculations, because the combustion chamber is not adiabatic: the outlet is not closed and radiation exchanges energy with hot gases in the atmosphere.

Fig. 5 shows the mean heat release and the radiative source term fields in the plane $z = 0$. Although the energy released by combustion is much more important in intensity (by about 2 orders of magnitude) the spatial distribution strongly differs (see the ratio $|S_r|$ /HR in Fig. 5). The energy released by combustion is located along the flame front where the gas is burning while the radiative source term is important in non reacting zones inside the burnt gas. Therefore, the impact of radiation strongly depends on the ratio between the flame surface and the volume of burnt gas.

Global volume quantities calculated for Y_{H_2O}, Y_{CO_2}, T, HR and P by integrating them over the whole domain for both coupled and uncoupled calculation are given in Tab. 1, together with the relative differences between the coupled and the uncoupled calculations. All are around 1%, showing that the impact of radiation on mean quantities is small and the reduced chemical stay valid for the main species and the temperature. The total mass fraction of CO is modified by 10% but such variation should be considered with caution in this analysis as CO is used in the reduced chemical scheme to fit the correct flame speed and temperature but may lead to non physical values of CO mass fraction outside the flame brush region. However minor species are known to be more sensitive to the temperature level [43, 44] and may be more impacted by radiation.

Looking now at local quantities absolute and relative difference fields are calculated for various mean variables and presented in Fig. 6. For a quantity

X, the absolute difference is defined as:

$$D(X) = X_{\text{coupled}} - X_{\text{uncoupled}} \tag{25}$$

while the relative difference is calculated as:

$$d(X) = \frac{X_{\text{coupled}} - X_{\text{uncoupled}}}{\max\left(X_{\text{uncoupled}}\right)} \tag{26}$$

Fig. 6 shows that radiation decreases the local temperature about 140 K near the flame front in the burnt gas side. In the fresh gas the temperature is locally increased by more than 100 K. Temperature RMS values are compared using the intensity of temperature fluctuations, defined as:

$$I\left(T_{RMS}\right) = \frac{T_{RMS}}{\widetilde{T}} \tag{27}$$

where $\widetilde{T}$ is the filtered temperature. In both cases the maximum temperature fluctuation intensity is around 85%. Taking into account radiation, the absolute difference on the intensity fluctuations is decreased by 10% in burnt gas and increased by 10% around the flame front. Temperature is modified by radiation: the burnt temperature T_1 is decreased while the cold temperature T_0 is increased. The heat release factor $\tau = (T_1/T_0) - 1$ is decreased producing an increase in the flame speed S_l^0 which enhances the flame sensitivity to turbulent motion.

The relative difference on the heat release shows that the maximum energy released by combustion can be decreased on the flame front by more than 15% but the flame brush is thickened by the inclusion of radiation. This is consistent with the increase of temperature fluctuations: the wrinkling of the flame front is larger so the mean reacting zone is thickened and the maximum time averaged value is decreased.

A very small impact is observed on the relative difference of velocity showing that the main dynamics of the flow is not altered by radiation. However the mass flow rate changes close to the flame front, due to dilatation of the gas in the zone where the temperature is modified. In the cold gas the mass flow rate is decreased by 8% and in the burnt gas it is increased by 4%. The impact on pressure is negligible.

The effect of radiation is limited on the mean dynamics of the flow, but is clearly visible on instantaneous solutions, as shown in Fig. 7 where fields

of temperature and velocity at the same time for the coupled and the uncoupled calculations. The computation including radiation shows larger turbulent structures (*i.e.* lower spatial frequencies). The effect of radiation on flow frequencies has already been observed in previous studies [45] and is confirmed here. Frequency analysis using FFT of temporal signals demand very long simulations because the characteristic frequency of the flow is low. A frequency-time analysis is preferred using a wavelet approach which gives quantitative information on the unsteadiness of the flow and is shown in Figs. 8 to 11. The wavelet power spectrum calculated for the y-component of the velocity is plotted in Figs. 8 and 9 and for the temperature in Figs. 10 and 10. The uncoupled calculation has two candidates for characteristic frequencies, the first in the range $128 - 256\ Hz$ and a second in the range $256 - 512\ Hz$. For the available sampling time, these two frequencies alternate in time. When including radiation the behavior of the system is different: the two frequency ranges are nearly merged. The lower frequencies are amplified as suggested by the instantaneous fields in Fig. 7. The temporal evolution of the high frequencies tends to be smoother when radiation is considered. This means that radiation modifies the turbulent distribution of energy (*i.e.* turbulence diffuses energy at higher frequencies): indeed radiation exchanges energy between hot and fresh gases and tends to homogenize the energy distribution. This is a first step into the analysis of the influence of radiative heat transfer on flow instabilities and should be confirmed on other configurations using a larger sampling time.

5. Influence of turbulence on radiation: Turbulence-Radiation Interaction (TRI) analysis

The problem of the Turbulence-Radiation Interaction has been studied for over two decades using theory, experiments and simulations and a detailed review on the subject has been written by Coelho [26]. When calculating the time averaged radiative source term, neglecting fluctuations can lead into large discrepancies due to the non linearity of the radiative term. This is the so-called TRI problem, first defined in the Reynolds Average Navier-Stokes (RANS) context.

One of the main difficulties encountered in the analysis of TRI consists in the recollection of representative time fluctuations of the different quantities in combustion problems. Experimental instantaneous fields are difficult to obtain for all flow quantities, so numerical simulation have been widely used

to generate them. At first some authors presumed the shape of the PDF to generate temperature fluctuations [46, 47]. Subsequently there were attempts to generate fluctuations along the lines of sight [26].

LES explicitly solves large turbulent fluctuations while the smallest eddies are modeled: the unsteady quantities of the flow are decomposed in a filtered value and a fluctuating part:

$$X = \widetilde{X} + X' \tag{28}$$

$$= \underbrace{\langle X \rangle + X''} + X' \tag{29}$$

where $\widetilde{X}$ is the LES spatially filtered value, X' is the subgrid scale fluctuation, $\langle X \rangle$ is the time-averaged value and X'' is the temporal fluctuation related to the filtered value.

In Eq. 29 the filtered value from LES (noted with a tilde) has been decomposed in a time averaged value and a fluctuating resolved part (noted with a double prime). Therefore it is possible to use LES to calculate explicitly all the TRI contributions over the whole domain using realistic resolved fluctuations (precedent studies [27, 5, 28, 29, 30] have shown that the influence of subgrid scale fluctuations X' could be neglected).

Only a few authors acknowledge the use of LES for TRI. Malalasekera *et al.* [48] used Discrete Transfer Method (DTM) with a Mixed Gray Gas Model to study a swirl jet flame of CH4/H2(1:1). They compared the TRI effects by time averaging LES results at 4 probe locations. Gupta *et al.* [49] also used LES to calculate TRI contributions with a P1-Gray model for radiation on non reacting turbulent planar channel. They performed a sensitivity analysis of the TRI with the gray optical thickness.

In this work a new approach is proposed: LES is used to explicitly calculate all the TRI contributions over the whole domain, for a real turbulent flame configuration, using a detailed radiation model (DOM) and an accurate global spectral model SNB-FSCK.

The radiative source term S_r given by Eq. (16) can be decomposed in two parts:

$$S_r = S_{r,e} - S_{r,i} \tag{30}$$

where $S_{r,e}$ is the emitted energy and $S_{r,i}$ the incident energy, defined as:

$$S_{r,e} = 4\sigma\kappa_P(T, X_i)T^4 \qquad (31) \qquad\qquad S_{r,i} = \int_0^\infty \kappa_\nu G_\nu d\nu \qquad (32)$$

where κ_p is known as the Mean Planck absorption coefficient and G is the incident radiation integrated over the solid angle.

The time averaged values of the flow quantities (e.g. temperature T and species molar fraction X_i) are extracted from the coupled simulation. From this mean solution the radiative fields of the mean flow are calculated: the radiative source term $S_r(\langle T\rangle, \langle X_i\rangle)$, the incident radiative energy $S_{r,i}(\langle T\rangle, \langle X_i\rangle)$, and the mean Planck absorption coefficient $\kappa_P(\langle T\rangle, \langle X_i\rangle)$. This gives radiative fields where no turbulent fluctuation is included (like mean fields obtained from a RANS simulation).

The differences between these radiative fields and mean radiative source terms (*i.e.* $\langle S_r(T, X_i)\rangle$), obtained from instantanous solutions of a coupled simulation, are due to the non-linearities of the radiative source term which can be decomposed as:

$$\begin{aligned}\langle S_r(T, X_i)\rangle =& S_{r,e}\left(\langle T\rangle, \langle X_i\rangle\right)\left(1 + R_{\kappa_P}\right)\left(1 + R_{T^4} + R_{I_b}\right) \\ &- S_{r,i}(\langle T\rangle, \langle X_i\rangle)\left(1 + R_G\right) \\ \neq& S_r\left(\langle T\rangle, \langle X_i\rangle\right)\end{aligned} \qquad (33)$$

where R_{κ_P}, R_{T^4}, R_{Ib} corresponding to the absorption auto-correlation, the temperature auto-correlation and the cross-correlation between temperature and absorption. In addition a new TRI quantity appears in the incident term, R_G, corresponding to the absorption correlation. These correlations are defined as:

$$\left.\begin{aligned} R_{\kappa_p} &= \frac{\langle\kappa_P(T,X_i)\rangle}{\kappa_P(\langle T\rangle,\langle X_i\rangle)} - 1 \\ R_{T^4} &= \frac{\langle T^4\rangle}{\langle T\rangle^4} - 1 \\ R_{I_b} &= \frac{\langle\kappa_P'(T^4)'\rangle}{\langle\kappa_P\rangle\langle T\rangle^4} \end{aligned}\right\} \text{Emission TRI} \qquad (34)$$

$$R_G = \frac{\langle S_{r,i}(T,X_i)\rangle}{S_{r,i}(\langle T\rangle,\langle X_i\rangle)} - 1 \quad : \text{Incident TRI} \tag{35}$$

$$R_{S_r} = \frac{\langle S_r(T,X_i)\rangle}{S_r(\langle T\rangle,\langle X_i\rangle)} - 1 \quad : \text{Total TRI} \tag{36}$$

In all these expressions it was assumed that temporal and spectral integration are commutative. In the literature R_{κ_P}, R_{T^4}, R_G and R_{S_r} are usually defined without the -1 term. In this work all the correlations have been defined to represent only the turbulent part and are zero in laminar zones.

The correlations have been reconstructed using the unsteady calculation by performing temporal averaging of S_r, $S_{r,i}$, κ_P (Fig. 12) and T^4. These values are computed from the radiative instantaneous solutions and take into account the effects of turbulence. In addition, an independent radiative calculation was carried out using a time averaged solution of the coupled LES solution. TRI quantities R_{κ_P}, R_{T^4} and R_G can be directly deduced from these fields, and the cross-correlation R_{Ib} can be reconstructed:

$$R_{I_b} = \frac{\langle S_{r,e}(T,X_i)\rangle}{S_{r,e}(\langle T\rangle,\langle X_i\rangle)}\frac{1}{R_{\kappa_P}} - R_{T^4} \tag{37}$$

The correlations calculated using Eq. (34) to (36) are plotted in Fig. 13. It is shown that absolute values of TRI reach important values, up to 100%. However absolute values are not representative of the influence of the TRI on the radiated energy: for example R_G is important beyond the flame holder where gases are transparent and S_r is weak) and . It is more convenient to normalize TRI correlations with the maximum emitted, incident and total energy such as:

$$\left.\begin{aligned} \widehat{R_{\kappa_p}} &= R_{\kappa_p} \\ \widehat{R_{T^4}} &= R_{T^4} \\ \widehat{R_{I_b}} &= R_{I_b} \end{aligned}\right\} \times \frac{\langle S_{r,e}(T,X_i)\rangle}{\max\langle S_{r,e}(T,X_i)\rangle} \tag{38}$$

$$\widehat{R_G} = R_G \times \frac{\langle S_{r,i}(T,X_i)\rangle}{\max\langle S_{r,i}(T,X_i)\rangle} \tag{39}$$

$$\widehat{R_{S_r}} = R_{S_r} \times \frac{\langle S_r(T,X_i)\rangle}{\max\langle S_r(T,X_i)\rangle} \tag{40}$$

The total radiative heat loss is 1.89 kW when turbulence is included and 1.76 kW when it is not. This corresponds to the relative difference of 7.4%, but even if the difference on total heat loss is moderate the distribution of S_r on Fig. 14 shows variations from -20% to $+20\%$.

The correlation R_{T^4} and R_{Ib} in Figs. 13 and 14 are the most important correlations. They are localized in the flame brush where the values of T_{RMS} are high (Fig. 3). The first one is positive while the second is negative leading to an equilibrium between the two terms, as discussed in a preceding paper [27].

Following the analysis proposed by Snegirev [50], a Taylor expansion of κ_P as a function of T and X_i can be performed. If the fluctuation intensity is low, higher order correlations may be dropped and the emission correlations R_{T^4} and R_{Ib} may be written as:

$$R_{T^4} \approx 6\frac{\langle T'^2\rangle}{\langle T^2\rangle} \tag{41}$$

$$R_{I_b} \approx 4\frac{1}{\langle\kappa_P(T,X_i)\rangle\langle T\rangle}\left(\langle T'^2\rangle\left.\frac{\partial\kappa_P}{\partial T}\right|_{\langle T\rangle}+\langle T'X'\rangle\left.\frac{\partial\kappa_P}{\partial X_i}\right|_{\langle X_i\rangle}\right) \tag{42}$$

The temperature auto-correlation is always positive (see Eq. 41). The cross correlation can be positive or negative as it depends on a term in $\frac{\partial\kappa_P}{\partial T}$ (Eq. 42), which is mainly negative.

Fig. 14 shows that the absorption auto-correlation R_{κ_P} and the incident correlation R_G are low (at the exception of the zone near the flame anchor Fig. 14). This two correlations have also an opposite effect and are linked because R_G contains a contribution of the absorption correlation (see Eq. 35 and 32). The net budget in Eq. 33 is positive as $R_{\kappa_P} \geq R_G$.

6. Application of TRI in the RANS context

Several approaches were developed for RANS applications to model the impact of TRI. The purpose is to reconstruct $\langle S_r(T,X_i)\rangle$ from the mean values $S_r(\langle T\rangle,\langle X_i\rangle)$ along with a model which describes TRI. These approaches can be tested using the different correlations calculated with LES.

The most classical approximation to model TRI consists in neglecting R_G using the so called "Optically Thin Eddy Approximation" (OTFA) [51]. This is the most difficult to model because it depends on a non local terms. So in

this first approach all the emission TRI correlations (*i.e.* R_{κ_P}, R_{T^4} and R_{Ib}) are considered but the incident TRI (*i.e.* R_G) is neglected.

In the literature different levels of description are used to describe emission TRI [26]: in the first level, (improperly) called "Full TRI", the absorption auto-correlation R_{κ_P} is assumed to be weak and only R_{T^4} and R_{Ib} are kept; in the second level, called "Partial TRI", only the temperature auto-correlation is evaluated.

Fig. 15 shows the relative error of the four approaches: OTFA only (R_G is neglected), OTFA–Full (R_G and R_{κ_P} are neglected), OTFA–Partial (only R_{T^4} is considered) and No TRI (all correlations are neglected). The relative error between the TRI models and the full coupled simulation is calculated using:

$$\epsilon_{\text{TRI}} = \left[\left(\frac{S_{r,e}(\langle T\rangle, \langle X_i\rangle)}{\langle S_{r,e}(T, X_i)\rangle} \times R - 1\right) + \left(\frac{S_{r,i}(\langle T\rangle, \langle X_i\rangle)}{\langle S_{r,i}(T, X_i)\rangle} - 1\right)\right] \times \frac{\langle S_r(T, X_i)\rangle}{\max \langle S_r(T, X_i)\rangle} \tag{43}$$

where the total correlation factor R is different for each model:

$$R = (1 + R_{\kappa_P})(1 + R_{T^4} + R_{I_b}) \quad : \text{OTFA only} \tag{44}$$

$$R = 1 + R_{T^4} + R_{I_b} \quad : \text{OTFA–"Full TRI"} \tag{45}$$

$$R = 1 + R_{T^4} \quad : \text{OTFA–"Partial TRI"} \tag{46}$$

$$R = 1 \quad : \text{No TRI} \tag{47}$$

Relative errors from Fig. 15 give the validity of each TRI model. As presented in Fig. 14 neglecting the incident TRI in the OTFA-Only approach gives errors around 10%. With the 3 other approaches OTFA-Full , OTFA-Partial and No-TRI the errors are similar showing that an uncomplete set of the emission TRI correlations (*i.e.* R_{κ_P}, R_{T^4} and R_{Ib}) is not sufficient. Tab.% 2 shows the same result on total radiative loss. Moreover the OTFA-Partial approach gives a higher error due to the unbalancing of the opposite contributions of R_{T^4} and R_{Ib}. The calculation of the total radiative loss given in Tab. 2 confirms these results.

TRI analysis on Fig. 13 and 14 from LES results shows that each correlation contribution is important. The correlations R_{T^4} and R_{Ib} are slightly more important but R_{κ_P} must not be neglected. The incident correlation R_G is slightly weaker but has the same order of magnitude than the other correlations. There are two compensations mechanisms, first between R_{T^4}

and R_{Ib} and second between R_{κ_P} and R_G. However the net contribution on R_{S_r} remains important close to the flame front and inside burning gases.

These results demonstrate the importance of radiative unsteady calculations even in cases where the modification of fluid dynamics caused by radiation is not studied. The temporal analysis of TRI from LES fluctuations shows that all the correlations are important and must be considered. Even more it shows that neglecting some terms can create an unbalance in the correlations leading to wrong radiative fields.

In RANS the TRI correlations are calculated (or modelled) from RANS turbulence models [26]. In LES it has been shown in this work that TRI correlations can be explicitly calculated from resolved fluctuations. This kind of analysis could also be used to build a model for the TRI correlations in the computation of $\langle S_r(T, X_i)\rangle$ using LES simulations instead of a RANS model.

7. Conclusions

A detailed study of the coupling between radiative heat transfer and LES of turbulent combustion in a real laboratory flame configuration has been presented.

It was shown that radiation impacts the structure of the flame brush. Although the radiative energy is 2 orders of magnitude lower than the heat release by combustion, radiative exchanges have a visible impact on the energy distribution. Radiation has a higher effect on local quantities compared to global quantities: the mean temperature in the domain decreases by 20 K with radiation, while extreme temperatures change between -150 K and $+150$ K (increase in fresh gas and decrease in burnt gas). This can have a significant effect on the prediction of minor species pollutants or soot and should be studied using detailed chemistry. These temperature changes have also an impact of the flame sensitivity to turbulent motion and increase of the flame fluctuations: the wrinkling of flame brush is stronger. The mean flow velocity is not altered but a variation on mean flow rate, due to dilatation, was detected. The unsteady evolution of the flow has been discussed using a time-frequency analysis with power spectrum wavelets. This analysis showed that peaks at characteristic frequencies are smoother and larger when radiation is present. Finally radiation tends to homogenize energy and frequency distribution of the flow.

The second part of the study focuses on the Turbulence Radiation Interaction (TRI) using the instantaneous radiative fields on the whole computation domain. This is the first work where TRI correlations are calculated over the whole domain on a real burner using unsteady turbulent fluctuations obtained from LES simulations. TRI correlations include: 3 emission correlations (absorption auto-correlation R_{κ_P}, temperature auto-correlation R_{T^4} and temperature absorption cross-correlation R_{Ib}) and one incident correlation (R_G).

The results show that Turbulence Radiation Interaction increases the total radiative heat loss by 7.4% and that at some points the radiative source term varies from -20% to $+20\%$. The relative importance of each correlation has been discussed using 4 levels of approximation used in literature: OTFA-Only (R_G neglected), OTFA–Full (R_{κ_P} and R_G neglected), OTFA–Partial (R_{κ_P}, R_{Ib} and R_G neglected) and No-TRI (all neglected), showing that all of the correlations have an important effect. All three emission TRI must be considered and the absorption auto-correlation can not be neglected. The incident TRI R_G is slightly less important but has the same order of magnitude than emission TRI. The TRI analysis is a first step towards TRI modeling in turbulent flames and this work constitutes a good basis to build radiative models including the TRI correlations for RANS simulations.

Acknowledgement

This work was granted access to the HPC resources of CINES under the allocation 2011- c2011026401 made by GENCI (Grand Equipement National de Calcul Intensif). We acknowledge A. Dauptain form CERFACS for his help on the unsteady analysis and the calculation of wavelets.

References

[1] M. Boileau, G. Staffelbach, B. Cuenot, T. Poinsot, C. Bérat, Combustion and Flame 154 (2008) 2–22.

[2] A. Roux, L. Gicquel, Y. Sommerer, T. Poinsot, Combustion and Flame 152 (2008) 154–176.

[3] G. Boudier, L. Gicquel, T. Poinsot, Combustion and Flame 155 (2008) 196–214.

[4] D. Joseph, Modélisation des transferts radiatifs en combustion par méthode aux ordonnées discrètes sur des maillages non structurés tridimensionnels, Ph.D. thesis, Institut National Polytechnique de Toulouse, 2004.

[5] D. Poitou, Modélisation du rayonnement dans la simulation aux grandes échelles de la combustion turbulente, Ph.D. thesis, Institut National Polytechnique de Toulouse, 2009.

[6] J. Amaya, Unsteady coupled convection, conduction and radiation simulations on parallel architectures for combustion applications, Ph.D. thesis, CERFACS, 2010.

[7] T. Poinsot, D. Veynante, Theorical and Numerical Combustion, Edwards, 2001.

[8] F. Ducros, F. Nicoud, T. Poinsot, in: B. M. J. (Ed.), Proc. 6th ICFD Conference on numerical methods for fluid dynamic, pp. 293–300.

[9] F. Nicoud, F. Ducros, Flow, Turbulence and Combustion 62 (1999) 183–200.

[10] T. Poinsot, S. Lele, Journal of Computational Physics vol.101 (1992) 104–129.

[11] O. Colin, M. Rudgyard, Journal of Computational Physics 162 (2000) 338–371.

[12] O. Colin, F. Ducros, D. Veynante, T. Poinsot, Physics of Fluids 12 (2000) 1843–1863.

[13] L. Selle, G. Lartigue, T. Poinsot, R. Koch, K.-U. Schildmacher, W. Krebs, B. Prade, P. Kaufmann, D. Veynante, Combustion and Flame 137 (2004) 489–505.

[14] D. Joseph, P. J. Coelho, B. Cuenot, M. E. Hafi, in: Eurotherm73 on Computationnal Thermal Radiation in Participating Media, volume 11, Eurotherm series, Mons (Belgium), pp. 97–106.

[15] D. Joseph, M. E. Hafi, R. Fournier, B. Cuenot, International Journal of Thermal Sciences 44 (2005) 851–864.

[16] K. A. Jensen, J. Ripoll, A. Wray, D. Joseph, M. E. Hafi, Combustion and Flame 148 (2007) 263–279.

[17] D. Joseph, P. Perez, M. E. Hafi, B. Cuenot, Journal of Heat Transfer 131 (2009) 052701–9.

[18] Truelove, Discrete-ordinate solutions of the radiation transport equation, J. S.(Univ. of Newcastle, 1987.

[19] R. Koch, R. Becker, Journal of Quantitative Spectroscopy and Radiative Transfer 84 (2004) 423–435.

[20] A. Soufiani, J. Taine, Technical note in International Journal of Heat and mass transfer 40 (1997) 987–991.

[21] V. Goutiere, F. Liu, A. Charette, Journal of Quantitative Spectroscopy and Radiative Transfer 64 (2000) 299–326.

[22] V. Goutière, A. Charette, L. Kiss, Numerical Heat Transfer Part B: Fundamentals 41 (2002) 361–381.

[23] D. Poitou, J. Amaya, C. Bushan Singh, D. Joseph, M. E. Hafi, B. Cuenot, in: Proceedings of Eurotherm83 – Computational Thermal Radiation in Participating Media III.

[24] F. Liu, M. Yang, G. Smallwood, H. Zhang, in: Proceedings of ICHMT, RAD04, Istanbul, Turkey.

[25] A. Soufiani, E. Djavdan, Combustion and Flame 97 (1994) 240 – 250.

[26] P. J. Coelho, Progress in Energy and Combustion Science 33 (2007) 311–383.

[27] D. Poitou, M. E. Hafi, B. Cuenot, Turkish Journal of Engineering and Environmental Sciences 31 (2007) 371–381.

[28] M. Roger, C. B. D. Silva, P. J. Coelho, International Journal of Heat and Mass Transfer 52 (2009) 2243 – 2254.

[29] P. J. Coelho, Combustion and Flame 156 (2009) 1099–1110.

[30] M. Roger, P. J. Coelho, C. B. da Silva, International Journal of Heat and Mass Transfer 53 (2010) 2897–2907.

[31] D. Poitou, M. El Hafi, , B. Cuenot, Journal of Heat Transfer 133 (2010) 062701–10.

[32] J. Amaya, O. Cabrit, D. Poitou, B. Cuenot, M. E. Hafi, Journal of Quantitative Spectroscopy and Radiative Transfer 111 (2010) 295–301.

[33] F. Duchaine, A. Corpron, L. Pons, V. Moureau, F. Nicoud, T. Poinsot, International Journal of Heat and Mass Transfer 30 (2009) 1129–1141.

[34] M. Lecanu, Couplage multi-physique combustion turbulente - rayonnement - cinétique chimique, Ph.D. thesis, École centrale Paris, 2005.

[35] Y. Wang, Direct Numerical Simulation of non-premixed combustion with soot and thermal radiation, Ph.D. thesis, University of Maryland, 2005.

[36] R. Gonçalves dos Santos, M. Lecanu, S. Ducruix, O. Gicquel, E. Iacona, D. Veynante, Combustion and Flame 152 (2008) 387–400.

[37] R. Gonçalves dos Santos, Large Eddy Simulation of Turbulent Combustion Including Radiative Heat Transfer, Ph.D. thesis, EM2C, 2007.

[38] T. Lagarde, A. Piacentini, O. Thual, Quarterly Journal of the Royal Meteorological Society 127 (2001) 189–207.

[39] G. Staffelbach, L. Y. M. Gicquel, T. Poinsot, Highly Parallel Large Eddy Simulations of Multiburner Configurations in Industrial Gas Turbines, volume Complex Effects in LES, Lecture Notes in Computational Science and Engineering, pp. 325–336.

[40] R. Knikker, D. Veynante, J. Rolon, C. Meneveau, in: Proceedings of the 10th international Symposium on Applications of Laser Techniques to Fluid Mechanics.

[41] R. Knikker, D. Veynante, C. Meneveau, Proceedings of the Combustion Institute 29 (2002) 2105–2111.

[42] C. Nottin, R. Knikker, M. Boger, D. Veynante, Symposium (International) on Combustion 28 (2000) 67–73.

[43] H. Guo, F. Liu, G. Smallwood, Ömer Gülder, Combustion Theory and Modelling 6 (2002) 173–187.

[44] F. Liu, H. Guo, G. J. Smallwood, M. El Hafi, Journal of Quantitative Spectroscopy and Radiative Transfer 84 (2004) 501–511.

[45] P. Schmitt, Thermally accurate LES of the stability-emission performance of staged gas-turbine combustion, Ph.D. thesis, Université Paul Sabatier, 2005.

[46] G. Cox, Combustion Science and Technology 17 (1977) 75–78.

[47] S. Burns, Turbulence radiation interaction modeling in hydrocarbon pool fire simulation, Technical Report, 1999.

[48] W. Malalasekera, M. Deiveegan, S. Sadasivuni, S. Ibrahim, in: Proceedings of Eurotherm83 – Computational Thermal Radiation in Participating Media III.

[49] H. Gupta A., Modest M. F., Journal of Heat Transfer 131(6):061704 (2009).

[50] A. Y. Snegirev, Combustion and Flame 136 (2004) 51–71.

[51] V. Kabashnikov, G. Kmit, Journal Applied Spectroscopy 31 (1979) 963–967.

Notations

DMFS	Diamond Mean Flux Scheme
DOM	Discrete Ordinate Method
DNS	Direct Numerical Simulation
FS-SNBcK	Full Spectrum SNBcK
FSK	Full Spectrum κ (*i.e.* FS-SNBcK)
FSCK	Full Spectrum Correlated κ
FVM	Finite Volume Method
LES	Large Eddy Simulation
OTFA	Optically Thin Fluctuations Approximation
PCS	Parallel Coupling Strategy
RANS	Reynolds Averaged Numerical Simulation
RTE	Radiative Transfer Equation
SNB	Statistcal Narrow Band
SNBcK	SNB with correlated κ model
TRI	Turbulence Radiation Interaction
WSGG	Weighted Sum of Gray Gases

List of Figures

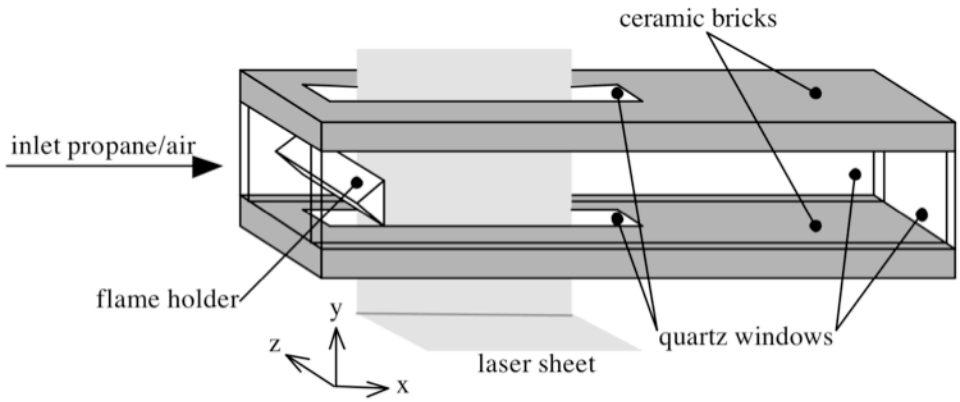

Figure 1: Strech of the configuration [40].

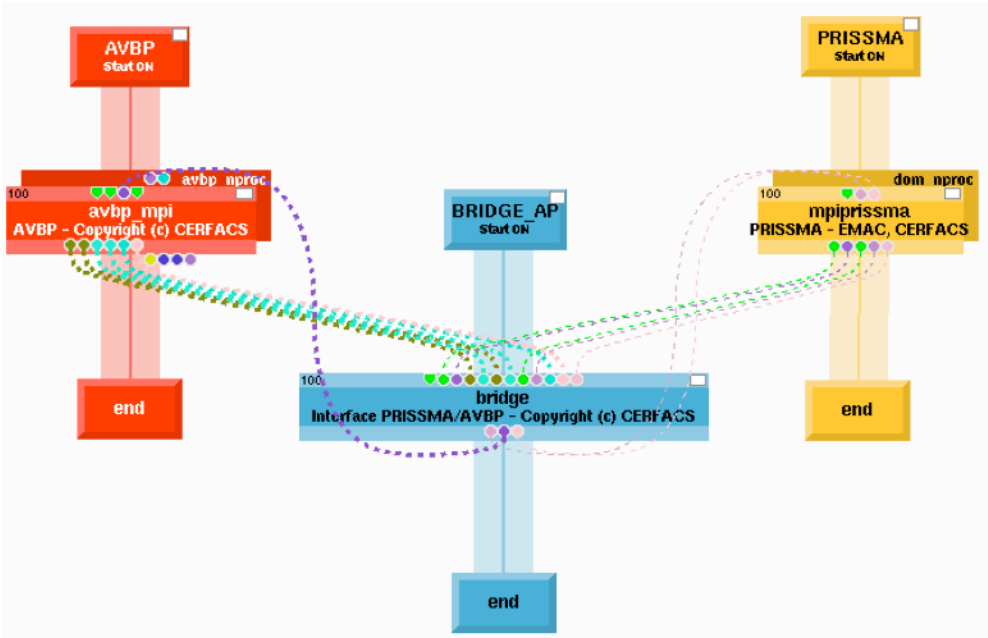

Figure 2: The O-PALM interface.

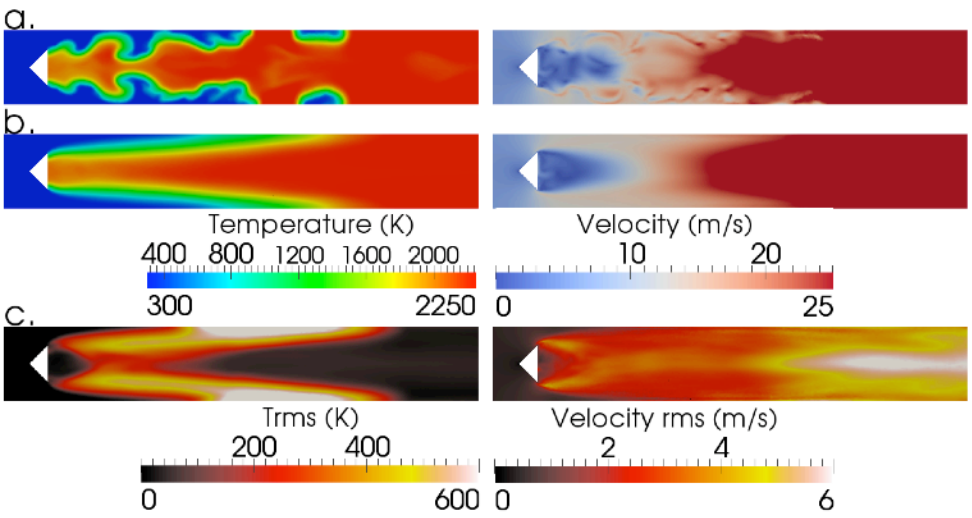

Figure 3: Fields of temperature and velocity in the plane $z = 0$ for the uncoupled calculation: a. instantaneous; b. Time averaged; c. RMS.

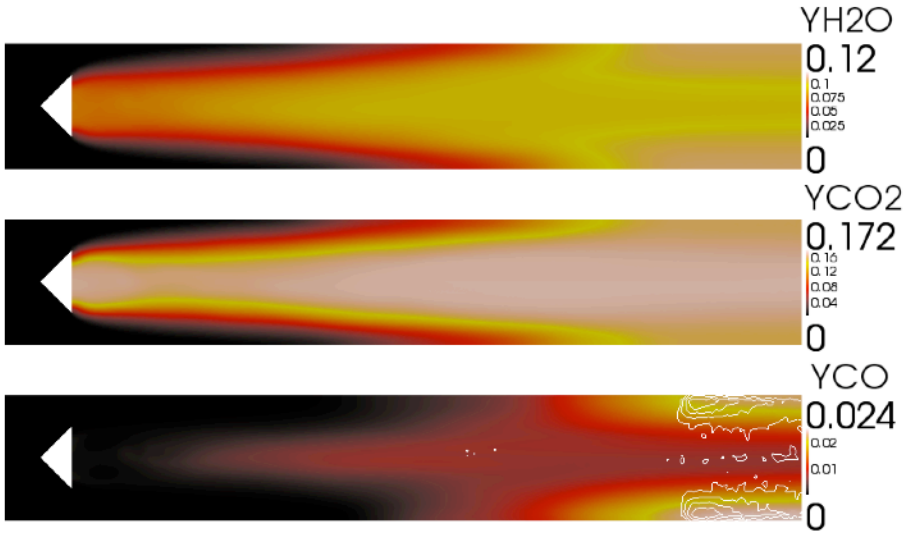

Figure 4: Time averaged fields of mass fraction of H_2O (top), CO_2 (middle) and CO (bottom) in the plane $z = 0$ for the uncoupled calculation. On the CO image, an isoline of negative reaction rate $\overline{\omega_2}$ is given.

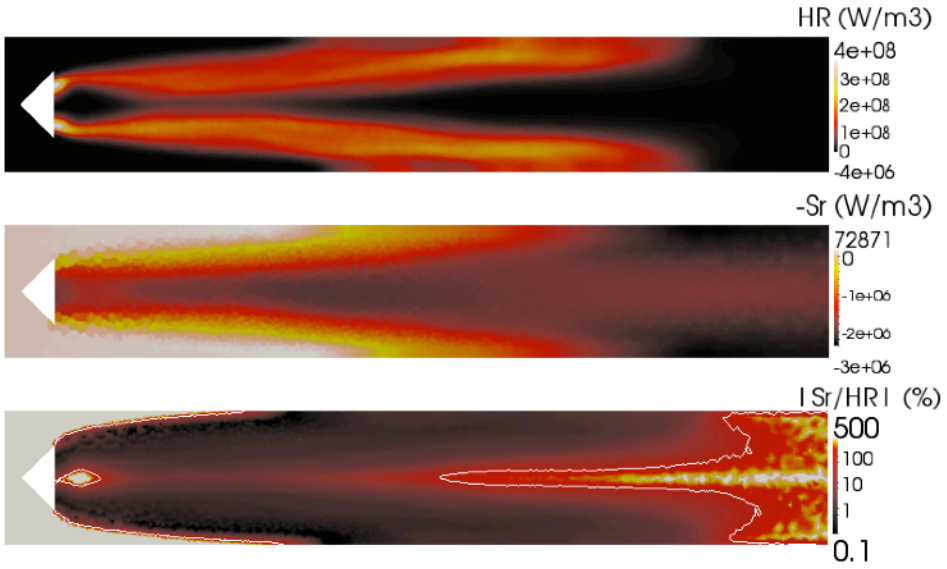

Figure 5: Time averaged fields of heat release (top) and radiative source term (middle) and norm of the relative contribution of Sr compared to HR ($|S_r/\mathrm{HR}|$) in percent with a contour at $|S_r| = \mathrm{HR}$ (bottom, logarithmic scale) in the plane $z = 0$ for the coupled calculation.

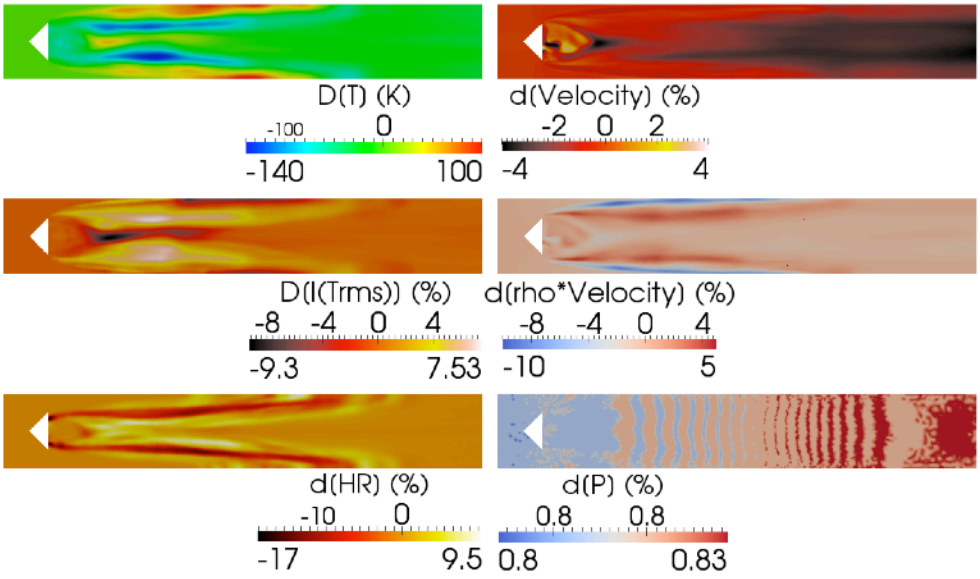

Figure 6: Absolute ($D(X)$) and relative ($d(X)$ in %) differences between coupled and uncoupled simulations for the time averaged temperature T, temperature intensity fluctuations $I(T_{RMS})$, heat release HR, velocity, mass flow rate $\rho \times u$ and pressure P.

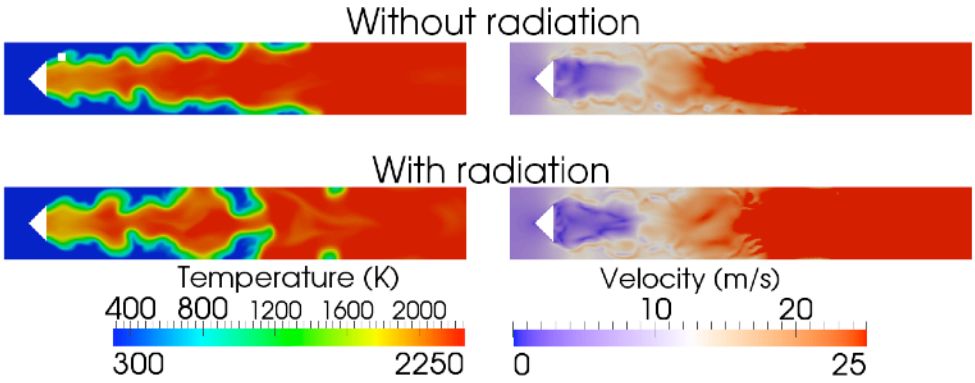

Figure 7: Instantanous fields of temperature for the uncoupled (top) and the coupled (bottom) simulations at $t = 0.5468817$ s. On the top figure the probe location for the spectral analysis ($x = 1$, $y = 1.5$, $z = 0$ cm) is represented by a white square.

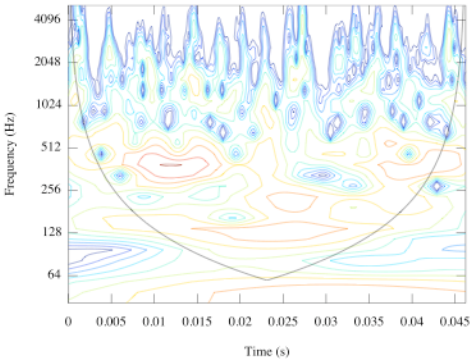

Figure 8: Time-frequency wavelet power spectrum of the y-component of the velocity in the uncoupled calculation. Structures under black line are not representative.

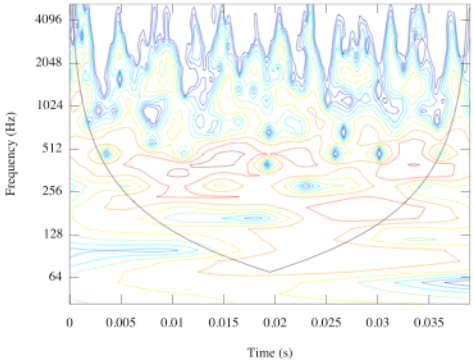

Figure 9: Time-frequency wavelet power spectrum of the y-component of the velocity in the coupled calculation. Structures under black line are not representative.

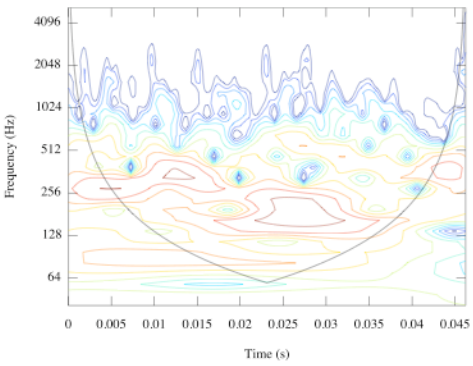

Figure 10: Time-frequency wavelet power spectrum of the temperature for the uncoupled calculation. Structures under black line are not representative.

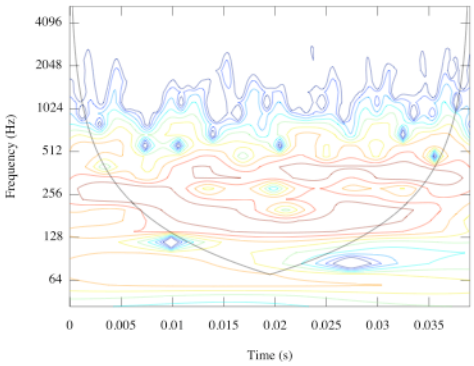

Figure 11: Time-frequency wavelet power spectrum of the temperature in the coupled calculation. Structures under black line are not representative.

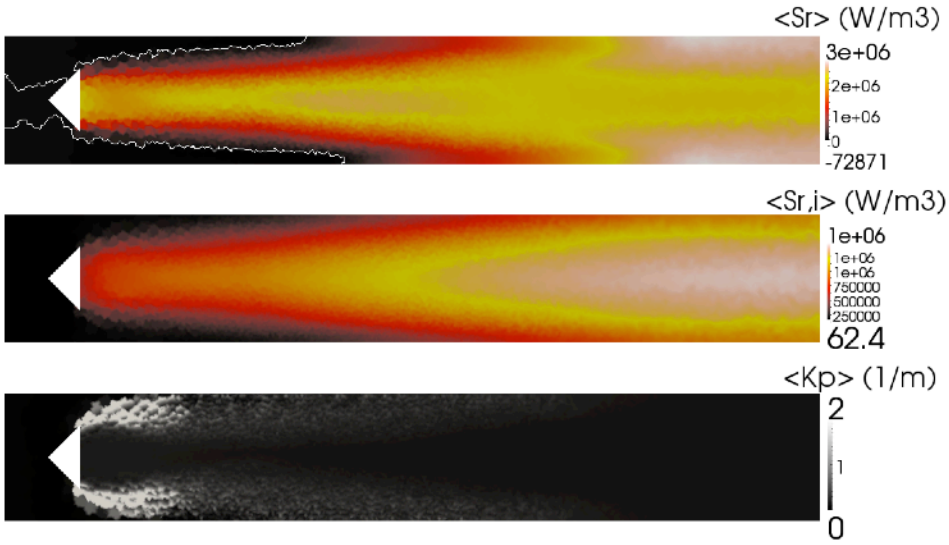

Figure 12: Time averaged fields for S_r (isoline at $S_r = 0$), $S_{r,i}$ and K_p in the plane $z = 0$.

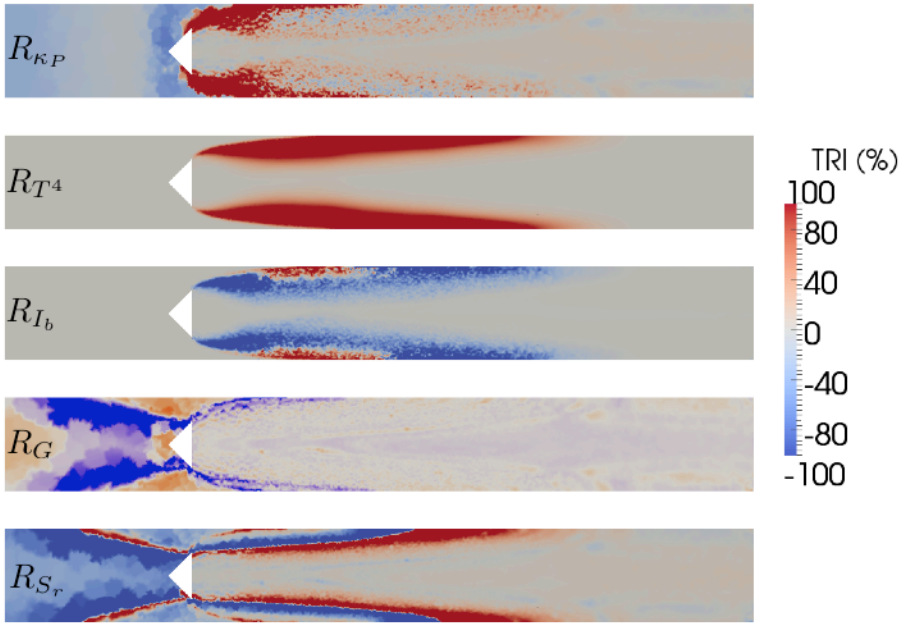

Figure 13: Turbulent correlations of the TRI: absorption auto-correlation R_{κ_P}, temperature auto-correlation R_{T^4}, temperature-absorption cross correlation R_{Ib}, incident correlation R_G, total correlation R_{S_r} in the plane $z = 0$.

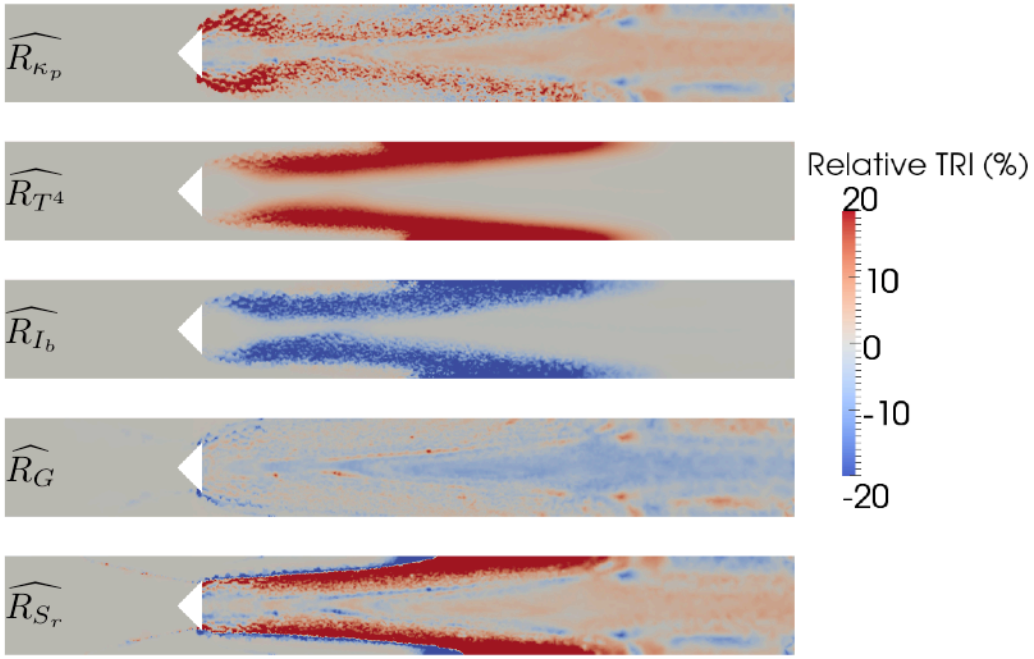

Figure 14: Scaled correlations of the TRI: absorption auto-correlation $\widehat{R_{\kappa_P}}$, temperature auto-correlation $\widehat{R_{T^4}}$, temperature-absorption cross correlation $\widehat{R_{Ib}}$, incident correlation $\widehat{R_G}$, total correlation $\widehat{R_{S_r}}$ in the plane $z = 0$. in the plane $z = 0$.

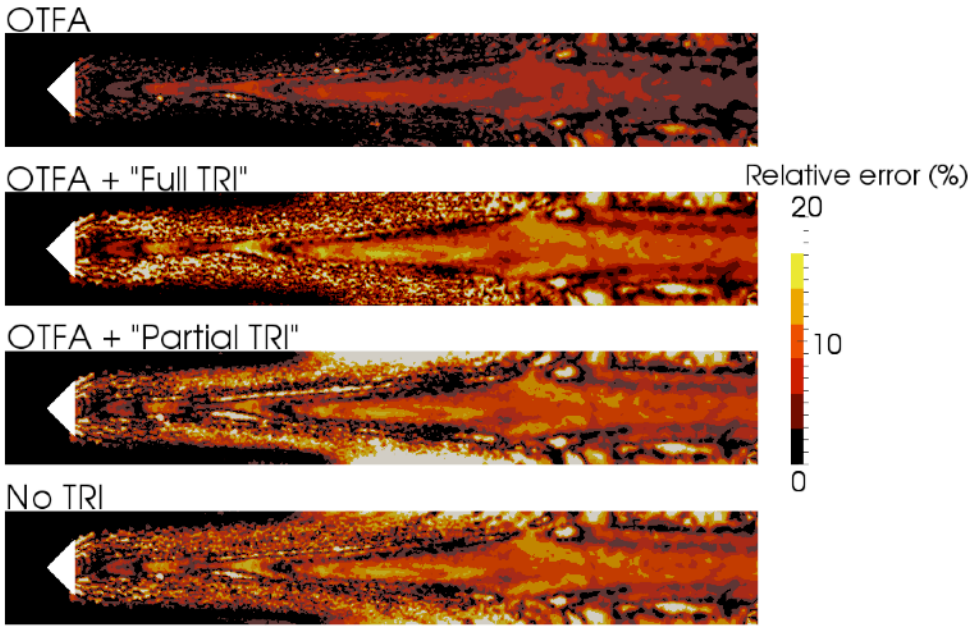

Figure 15: Evaluation of the different approaches developed in RANS context using correlations calculated from LES. OTFA: R_G is neglected; OTFA + "Full TRI": R_G and R_{κ_P} are neglected; OTFA + "Partial TRI": only R_{T^4} is considered; No TRI: all correlation are neglected.

List of Tables

	Uncoupled	Coupled	Relative difference (%)
Y_{H_2O}	$5.47 \cdot 10^{-2}$	$5.43 \cdot 10^{-2}$	-0.67
Y_{CO_2}	$9.36 \cdot 10^{-2}$	$9.37 \cdot 10^{-2}$	0.12
Y_{CO}	$5.19 \cdot 10^{-3}$	$4.70 \cdot 10^{-3}$	-9.45
T (K)	1435.32	1417.27	-1.26
HR (kW/m^3)	76.38	76.04	-0.45
P (Pa)	$1.21 \cdot 10^5$	$1.22 \cdot 10^5$	0.82

Table 1: Influence of radiation on total quantities integrated over the whole domain and relative difference between the two simulations.

	Total Radiative losses (kW)	Relative Difference (%)
All correlations	1.89	–
OTFA	1.92	+1.64
OTFA + "Full TRI"	1.80	−5.08
OTFA + "Partial TRI"	2.07	+9.16
No TRI	1.76	−6.88

Table 2: Influence of the RANS approaches on the total radiative loss.